

SalFormer360: a transformer-based saliency estimation model for 360-degree videos

Mahmoud Z. A. Wahba, *Graduate Student Member, IEEE*, Francesco Barbato, *Member, IEEE*,
Sara Baldoni, *Member, IEEE*, and Federica Battisti, *Senior Member, IEEE*

Abstract—Saliency estimation has received growing attention in recent years due to its importance in a wide range of applications. In the context of 360-degree video, it has been particularly valuable for tasks such as viewport prediction and immersive content optimization. In this paper, we propose SalFormer360, a novel saliency estimation model for 360-degree videos built on a transformer-based architecture. Our approach is based on the combination of an existing encoder architecture, SegFormer, and a custom decoder. The SegFormer model was originally developed for 2D segmentation tasks, and it has been fine-tuned to adapt it to 360-degree content. To further enhance prediction accuracy in our model, we incorporated Viewing Center Bias to reflect user attention in 360-degree environments. Extensive experiments on the three largest benchmark datasets for saliency estimation demonstrate that SalFormer360 outperforms existing state-of-the-art methods. In terms of Pearson Correlation Coefficient, our model achieves 8.4% higher performance on Sport360, 2.5% on PVS-HM, and 18.6% on VR-EyeTracking compared to previous state-of-the-art.

Index Terms—Saliency estimation, Omni-directional video, Viewing bias, Transformers.

I. INTRODUCTION

In recent years, Virtual Reality (VR) has gained widespread popularity, providing users with highly immersive experiences and allowing them to feel as if they were in a virtual world distinct from reality.

Omnidirectional images and videos have become one of the most popular content types for VR, thanks to the availability of user-friendly and low-cost 360-degree cameras. This content allows users to be placed at the center of a sphere and freely explore the environment in any direction by simply moving their heads. Although 360-degree media allows increased user immersion, their processing and transmission still entails many challenges. One major issue is the high memory and bandwidth requirements with respect to standard 2D content. For example, streaming a 4K 2D video requires approximately 25 Mb/s, while delivering a 4K resolution for each eye to provide a full 360-degree viewing experience requires around 400 Mb/s [1].

One effective way to address the transmission challenges of 360-degree videos is to implement a user-centered streaming

This work was partially supported by the European Union under the Italian National Recovery and Resilience Plan (NRRP) Mission 4, Component 2, Investment 1.3, CUP C93C22005250001, partnership on “Telecommunications of the Future” (PE00000001 - program “RESTART”) and by the European Union’s Horizon Europe Program under Agreement 101135637 (HEAT Project).

M. Z. A. Wahba, F. Barbato, S. Baldoni, and F. Battisti are with the Department of Information Engineering, University of Padova, Via Gradenigo 6b, 35131, Padua, Italy. (Corresponding author e-mail: sara.baldoni@unipd.it).

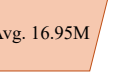
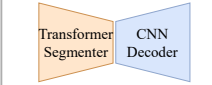
	Input Frames	Architecture	Parameters
Others	 # of frames ≥ 5	 RNN GNN Reinforcement Learning	
Ours	 # of frames = 2		

Fig. 1: SalFormer360 can estimate future salient points in 360-degree videos using only a single previous frame and with limited computational resources.

paradigm. To this aim, human attention mechanisms have been studied to design saliency estimation methods. These algorithms compute 2D probability maps which highlight the regions inside a 360-degree scene most likely to draw users attention [2]. These maps can then be used to transmit the salient regions at higher quality while encoding at lower quality (or discarding) less relevant areas [3].

Another possibility to reduce the transmission burden of 360-degree content considers the limitations of the human visual system, reflected by the Head-Mounted Displays (HMDs). Indeed, despite the availability of 360-degree content, users only see a portion of the frame at a time, which constitutes about 20% of the entire content [4]; the visible portion of a scene is commonly referred to as viewport. Based on this, saliency estimation and other cues, such as user previous head orientations and, in some cases, motion information, can be combined to predict the future viewports spanned by the users [5]–[11]. Viewport prediction can be integrated into streaming pipelines by delivering the predicted viewport in high quality, while downsampling or omitting peripheral regions. Compared to using head orientation alone, the integration of saliency maps enhances the accuracy of viewport prediction, enabling reliable forecasts over longer horizons (*e.g.*, up to 5 seconds) as shown in [5]. These observations highlight that accurate saliency estimation can foster efficient and effective streaming of 360-degree videos.

Saliency estimation has been extensively studied in the context of 2D images and videos, where it plays a crucial role in applications such as object detection and video compression. With the rapid growth of immersive media, research in this area has now expanded towards 360-degree content. This shift

presents new challenges due to the spherical geometry, larger field of view, and diverse viewing behaviors of users.

Our approach (summarized in Fig. 1) is motivated by the observation that segmentation models are trained to detect and isolate objects within a scene, and saliency models tend to highlight regions of interest that often correlate strongly with those objects. We leverage this relationship by adopting the transformer-based, 2D segmentation encoder Segformer [12] for our saliency estimation task. We feed 360-degree video frames into the Segformer encoder and exploit a custom decoder and viewing bias to generate the saliency maps.

Our contributions can be summarized as follows:

- We introduce SalFormer360, a novel transformer-based model for saliency estimation. Building on the SegFormer backbone originally developed for 2D segmentation tasks, we fine-tune the encoder and design a custom decoder before training the whole model on 360-degree video datasets to produce high-quality saliency maps.
- We account for human exploration behaviour by introducing a viewing bias to enhance the accuracy of saliency estimation.
- We extend two 360-degree datasets: PVS-HM [13] and VR-EyeTracking [14]. We generated ground-truth saliency maps from head orientation data and extracted RGB frames from MP4 videos, thus making them more accessible for future research in saliency estimation¹.
- We conduct extensive experiments on the three largest benchmark datasets for 360-degree videos: Sport360 [15], PVS-HM [13], and VR-EyeTracking [14]. Our model outperforms state-of-the-art competitors, achieving an improvement in CC of 8.34% in Sport360, of 2.60% in PVS-HM, and of 18.60% in VR-EyeTracking in terms of Pearson Correlation Coefficient (CC) compared to the best previously reported results.

The remainder of the paper is organized as follows: Section II reviews related work on saliency estimation. Section III provides a detailed description of our proposed model. Sections IV and V outline the experimental setup, the results, and provide ablation studies. Finally, Sections VI and VII discuss future directions and offer conclusive remarks.

II. RELATED WORK

In this section, we review the scientific literature concerning saliency estimation both for 2D and 360-degree content.

A variety of saliency estimation models have been proposed for traditional images and videos. For instance, in [16] transformers and Convolutional Neural Networks (CNNs) have been combined to predict saliency maps from static images.

In the video domain, TASED-Net [17] used a 3D convolutional encoder-decoder architecture. The encoder extracts spatial and temporal features from input frames, while the decoder reconstructs saliency maps based on the encoded representation. STSA-Net [18] introduced a spatio-temporal self-attention 3D network that incorporates multiple self-attention modules between 3D convolutional layers to capture long-range temporal dependencies between frames. Similarly, [19]

and [20] proposed Convolutional Long Short-Term Memory (Conv-LSTM) frameworks that integrate CNNs with Long Short-Term Memory (LSTM) units and attention mechanisms to model temporal dynamics more effectively. Furthermore, Droste *et al.* [21] developed the UNISAL model, which utilizes the lightweight MobileNet [22] architecture to facilitate efficient saliency estimation in both image and video domains.

Many studies have been devoted to 360-degree saliency estimation for both images and videos. For static 360-degree images, some approaches employed feature-based methods such as [2] [23], while more advanced methods used deep learning. Nguyen *et al.* proposed PanoSalNet [24], which uses CNN layers specifically designed for 360° images. This method has been included in viewport prediction pipelines in many approaches, such as [25] [26]. Similarly, SALGAN360 [27] adapted the 2D saliency model SALGAN [28] by fine-tuning it with 360° data, using a Graph Neural Network (GNN) [29] to predict saliency maps. In [30] an encoder-decoder architecture with spherical convolutions has been employed. Spherical convolutions have been presented in [31] and consist of redefining the kernels to account for the distortions in the equirectangular projection, effectively modeling the geometry of omnidirectional images.

In 360-degree videos, models typically integrate spatial and temporal features. Incorporating the concept of spherical convolutions, Sphere-GAN [32] introduces a Generative Adversarial Network (GAN)-based approach, where the generator consists of a U-Net [33] that employs spherical convolutions, while the discriminator uses standard conventional CNN layers. Additionally, Sphere-GAN predicts the saliency map at time t using the current equirectangular frame and the ground truth saliency map from time $t - 5$.

As an alternative approach, CP360 [34] projected the equirectangular frames in cubemap format and then applied CNN layers combined with Conv-LSTM [35] to capture spatio-temporal dependencies. Reinforcement learning (RL) has also been introduced to estimate saliency maps offline while simultaneously predicting viewport trajectories online [13]. SphereU-Net [36] extended the U-Net framework with an alternative version of spherical convolutions, where kernels are defined on spherical crowns and shifted across the sphere to respect the spherical geometry. A spherical 3D CNN-based model has been proposed in [37], where outputs were fused with center and initial frame biases for better prediction.

Attention mechanisms have also been exploited. ATSAL [38] incorporated an attention module to encode global static spatial features in the equirectangular domain, while simultaneously using an expert module on local cubemap patches across frames, fusing the outputs for final saliency estimation. Another valuable approach is SPVP360 [39], which combines spherical CNNs with a dual encoder-decoder design, featuring one stream for spatial features and one for temporal ones. The output of the two branches are then fused through an attention mechanism. In [40], another dual-stream framework used spherical Conv-LSTM and attention modules to process forward and backward frame sequences, with Gaussian bias maps added during post-processing. In SVGC-AVA [41], the authors proposed a model based on spherical vector-based

¹Code and resources available at: <https://github.com/LTTM/SalFormer360>

graph convolutions and audio-visual attention, where visual and audio features were extracted in the spherical domain.

Another option consists in incorporating optical flow information. The authors of [42], propose a framework combining cubemap projections with optical flow, where spatial and temporal features were extracted using CNNs and refined via a bidirectional Conv-LSTM-based saliency module. In addition, SST-Sal [43] introduced an encoder-decoder model that integrates optical flow with spherical Conv-LSTM layers to capture spatio-temporal dynamics. Optical flow is employed also in 360Spred [44], where a U-Net architecture and a 3D separable graph convolutional network [45] are used. 360Spred takes spherical frames and spherical optical flows as inputs. These optical flows are computed directly in the spherical domain using a spherical graph-based approach. This framework effectively extracts both visual and motion features within the sphere domain and leverages temporal correlations across both high-level and low-level spatial features.

Although many saliency estimation methods have tried to tackle saliency estimation for 360-degree videos, several limitations still exist. Many approaches rely on spherical convolutions or on converting equirectangular frames to cubic projections to address geometric distortions, thus introducing computational overhead. Additional complexity arises from the use of optical flow for motion-aware saliency estimation or from the processing of long temporal sequences (*e.g.*, more than 10 frames [40], [46]). Although these techniques can preserve temporal consistency, they significantly increase computational complexity and do not always lead to proportional improvements in performance.

In contrast to prior works that rely on computationally expensive solutions, we propose a lightweight transformer-based model, SalFormer360, that takes full advantage of the transformers' powerful ability to capture long-range dependencies and global contextual relationships [47] within 360-degree video content. Using this capability, our model efficiently learns both spatial and temporal correlations using only two frames (the current frame and the one at $t - 5$). By integrating viewing bias and a customized decoder, SalFormer360 outperforms state-of-the-art saliency prediction methods on 360-degree video benchmarks, confirming the representational power of transformer architectures while maintaining low computational complexity.

III. SALFORMER360 MODEL

In 2D images and videos, the Field of View (FoV) is fixed, making saliency estimation relatively straightforward. In contrast, in 360-degree videos, users can freely explore any direction within the scene, increasing the complexity of the saliency estimation and prediction.

Given a sequence of 360-degree video frames $\mathbf{I} \in \mathbb{R}^{T \times C \times H \times W}$, where T is the number of frames, C is the number of channels, and $H \times W$ is the spatial resolution, the objective is to predict the corresponding saliency maps $\mathbf{S} \in [0, 1]^{T \times 1 \times H \times W}$ highlighting regions of interest, which are likely to attract user attention.

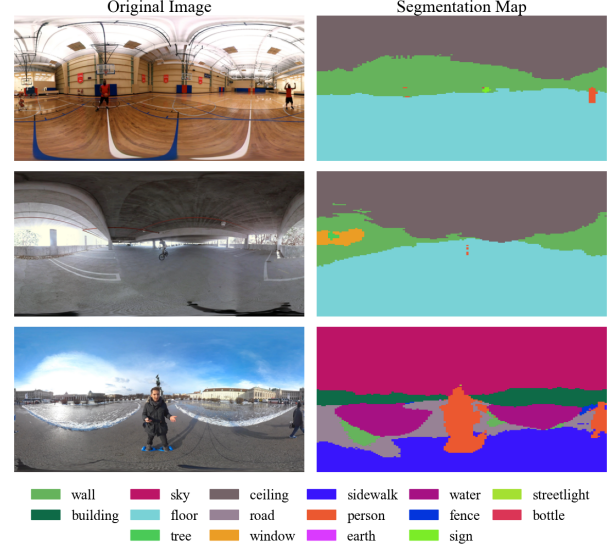


Fig. 2: Segmentation results obtained by feeding 360-degree equirectangular frames into the SegFormer-B0 model.

A. Network Structure

Let \mathbf{I}_t and \mathbf{I}_{t-k} represent the input frame sequences at time t and $t-k$, respectively. The objective is to predict the saliency map \mathbf{S}_t for frame t . This goal can be formulated as:

$$\mathbf{S}_t = \mathcal{M}(\mathbf{I}_t, \mathbf{I}_{t-k}), \quad (1)$$

where \mathcal{M} denotes the saliency estimation model that takes both the current and the previous frame as input.

To tackle the task of saliency estimation in 360-degree videos, we employ a transformer-based architecture that effectively captures both local and global spatial features. Specifically, we utilize the encoder of the SegFormer model [12] due to its efficiency and ability to extract detailed spatial representations through multiscale feature learning. The encoder was fine-tuned in conjunction with a custom decoder, designed to generate saliency maps from the 360-degree frame inputs.

As SegFormer was originally designed and trained for semantic segmentation on 2D images, we conducted an initial experiment to verify its suitability for 360-degree content. Specifically, our task involves processing 360-degree frames represented in equirectangular format. This projection introduces geometric distortions, especially near the poles, due to the transformation from spherical to planar coordinates. To assess the impact of geometric distortions on SegFormer's performance in segmentation tasks, we input the equirectangular frames into the lightweight SegFormer-B0 model, without applying any architectural modification, and qualitatively evaluate the output. This version of the segmenter was trained on ImageNet-1K [48] and fine-tuned on ADE20K [49].

Figure 2 presents three examples of omnidirectional image segmentation obtained by using SegFormer. The model shows a strong ability to recognize meaningful visual content, successfully identifying objects such as people, sky, and floor, despite projection-related distortions. This observation vali-

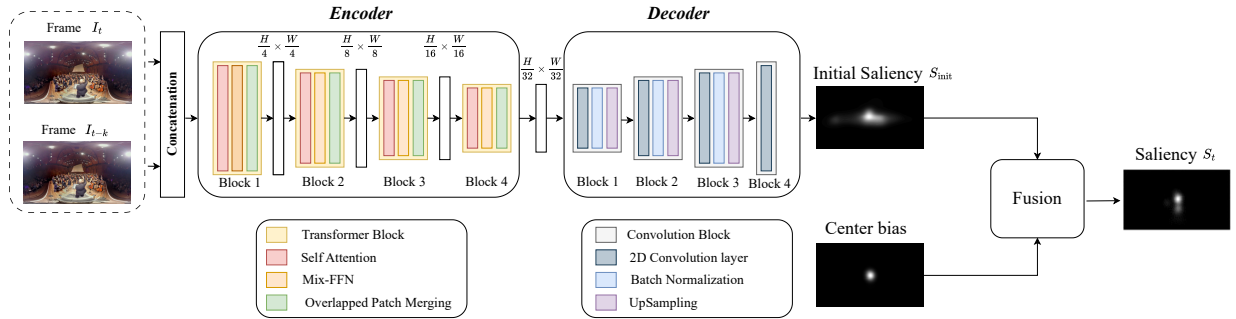


Fig. 3: Overview of the proposed 360-degree saliency estimation framework.

dates the potential of using SegFormer as an effective feature extractor for our task.

Building on this foundation, we adopt the pre-trained and fine-tuned MiT-B0 encoder as the backbone of our model. To adapt it for the specific challenges of saliency estimation in 360-degree videos, we design a custom decoder that utilizes the features extracted by the encoder to produce an initial saliency map. This initial prediction is then adaptively fused with a Center Bias (CB) to generate the final saliency output. The viewing bias CB accounts for the tendency of human observers to focus on the center of the 360-degree frame, as will be detailed in Section 4. Figure 3 shows the overall architecture of our proposed framework. In the following sections, we provide a detailed explanation of each component.

1) *Encoder*: For our model, we adopt the encoder component of SegFormer-B0 (MiT-B0), which implements a hierarchical transformer architecture composed of multiple stages. Each stage includes a transformer block that reduces spatial resolution through overlapping patch embeddings and then applies self-attention and feedforward layers. While the original SegFormer encoder is designed to process a single RGB image (with 3 channels), we modified it to handle two inputs, the current frames at time t and the frame at time $t - k$. We concatenated the two frames along the channel dimension, resulting in a 6-channel input. To this aim, we adapted the first convolutional layer of the encoder to accept 6 channels by duplicating the pre-trained weights for the first 3 channels. After processing the input through the encoder, we obtain a set of feature maps that effectively capture the spatial structure and semantic content of the 360-degree video frames.

2) *Decoder*: The proposed decoder architecture is specifically tailored to the generation of 360-degree saliency maps. Our decoder takes as input the feature map provided by the last stage of the encoder, which has the lowest spatial resolution. This feature map is passed through a sequence of three convolution layers, each followed by batch normalization, a ReLU activation function, and an upsampling layer using bilinear interpolation. Following this sequence, an additional final convolutional layer uses a sigmoid activation function to produce the initial saliency map (S_{init}). Furthermore, to improve generalization and prevent overfitting, during training we apply dropout with a rate of 30% throughout the decoder.

3) *Viewing Center Bias*: When users begin watching 360-degree videos, the headset typically starts by displaying the

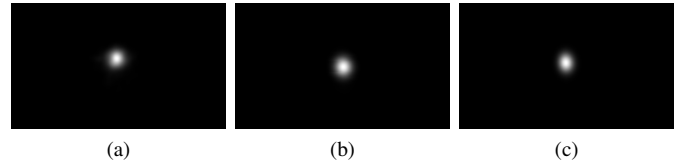


Fig. 4: Viewing Center Bias (CB), refer to Sec. III-A3 for details. (a) PVS-HM dataset, (b) Sport360 dataset, (c) VR-EyeTracking dataset.

same default viewport, meaning that the same longitude and latitude coordinates are shown at the beginning for all users. The device configuration and setup determine this starting viewpoint. Inspired by the approach proposed in [46], we computed the average ground truth saliency map of the first frame in all (training) videos in our 3 datasets, resulting in a representative image referred to as the CB, as illustrated in Figure 4. This CB captures the common visual focus present at the beginning of the 360-degree video playback. Moreover, our experiments and previous literature [40], [42], [46], show that this viewing bias is present throughout the video experience, making it an important component for saliency estimation models in 360-degree content. However, as the user is free to explore the content in all viewing direction, over time the CB decreases [46]. This means that the CB contributes more to the estimation of the saliency of the initial frames, and contributes less as the frame number increases. Therefore, we incorporated the CB into our model using the combination of a fixed term and a decaying function. The latter is guided by learnable parameters, which are optimized during the training process.

Formally, the estimation of the final saliency map (S) with the biasing operation can be described as:

$$S = w_t \cdot \mathbf{CB} + (1 - w_t) \cdot S_{init}, \quad (2)$$

where S_{init} is the unbiased saliency prediction for frame t , and w_t is a time-dependent weighting factor calculated as follows:

$$w_t = (1 - \beta_i)\delta(t) + \beta_i. \quad (3)$$

Here, t denotes the current frame index, $\delta(t) = e^{-\alpha_i(t/C)^2}$ is the function guiding the dynamics of the biasing [37], α_i and β_i are learnable parameters trained along with the model,

where i indicates the dataset used for training the model, and $C = 600$ is a constant.

It is useful to note that, thanks to the separation between dynamic and static components of the weighting factor, our approach can effectively model long and short-range biasing concurrently. The short-term bias is modeled by the dynamic function $\delta(t)$, which encodes the fact that the center bias is more prominent in the initial frames. As the frame index increases, δ gradually decays towards zero, mimicking the users' exploration behavior. In some videos, a subtle bias towards the center of the scene remains, and this is addressed by the long-term bias, controlled by the static parameter β_i , which remains constant in time. Both bias components are adaptively controlled by learnable parameters (α_i and β_i), which regulate the strength of the short-term and long-term biases, respectively. These parameters, different for each dataset, are optimized during training, allowing the model to adjust its biasing behavior to the specific viewing tendencies present in the data.

B. Loss Function

To train our model, we used a loss function as a combination of four different losses: Pearson linear correlation coefficient loss \mathcal{L}_{CC} , Kullback-Leibler divergence loss \mathcal{L}_{KL} , Spherical Mean Squared Error loss \mathcal{L}_{SMSE} , and Binary Cross Entropy loss \mathcal{L}_{BCE} . The final loss is illustrated in equation 4:

$$\mathcal{L} = \mathcal{L}_{CC}(\hat{\mathbf{S}}, \mathbf{S}) + \mathcal{L}_{KL}(\hat{\mathbf{S}}, \mathbf{S}) + \mathcal{L}_{SMSE}(\hat{\mathbf{S}}, \mathbf{S}) + \mathcal{L}_{BCE}(1, \mathbf{S}), \quad (4)$$

where $\hat{\mathbf{S}}$ denotes the ground truth saliency map, while \mathbf{S} represents the predicted saliency map. The Pearson linear correlation coefficient loss is defined as $\mathcal{L}_{CC}(\hat{\mathbf{S}}, \mathbf{S}) = 1 - CC(\hat{\mathbf{S}}, \mathbf{S})$, where CC is the Pearson linear correlation coefficient that measures the linear correlation between the predicted and ground truth saliency maps. The Kullback-Leibler divergence loss is defined as $\mathcal{L}_{KL}(\hat{\mathbf{S}}, \mathbf{S}) = KL(\hat{\mathbf{S}}, \mathbf{S})$, which quantifies the difference between the predicted saliency distribution and the ground truth. The Spherical Mean Squared Error loss is defined as $\mathcal{L}_{SMSE}(\hat{\mathbf{S}}, \mathbf{S}) = \Psi(\theta, \phi) \times MSE(\hat{\mathbf{S}}, \mathbf{S})$ where MSE represents the mean squared error, and $\Psi(\theta, \phi)$ represents the spherical weights that allow giving more importance to regions near the equator and lower weights to areas located near the poles. The \mathcal{L}_{SMSE} accounts for geometric distortions in equirectangular projections by penalizing prediction errors while respecting spherical geometry. Finally, the Binary Cross Entropy loss \mathcal{L}_{BCE} is a pixel-wise loss function that compares the predicted saliency map with the ground truth, focusing on accurately locating salient points.

IV. EXPERIMENTAL RESULTS

A. Dataset

To train and test our model, we used the three largest open-source datasets for saliency estimation and viewport prediction: PVS-HM [13], Sport360 [15], and VR-EyeTracking [14].

The PVS-HM dataset consists of 76 360-degree videos, varying from 20 to 80 seconds, with different resolutions

from 3K to 8K. These videos were viewed by 58 participants using the HTC VIVE HMD. The dataset includes various content types, such as gaming, sports, animation, driving, and natural scenes. The dataset contains MP4 videos and the corresponding head orientations of the viewing users.

The Sport360 dataset contains 104 360-degree videos, with durations ranging from 20 to 60 seconds, focusing on five different types of sports. This dataset was created thanks to the participation of 20 users who viewed the videos using the HTC VIVE equipped with the 7invensun a-Glass eye tracker. The dataset provides the RGB frames, the ground truth saliency maps, and the original gaze points of the viewers.

The VR-EyeTracking dataset consists of 208 360-degree videos varying from 20 to 60 seconds, covering a wide range of content, including documentaries, sports, and various indoor and outdoor scenes. Each video was watched by 45 participants using the HTC VIVE headset paired with the 7invensun a-Glass eye tracker. The dataset contains MP4 videos along with the eye fixation data and head orientations of the users.

We divided each dataset into training and testing sets. For the PVS-HM dataset, 61 videos were used for training, while 15 were set aside for testing. The Sport360 dataset was split into 80 videos for training and 24 for testing. Lastly, the VR-EyeTracking dataset was divided into 134 videos for training and 74 for testing. This splitting process followed the original methods outlined by the authors of each dataset.

Saliency maps generation: To customize the PVS-HM and VR-EyeTracking datasets for our task, we generated RGB frames from the MP4 videos using FFmpeg7.0.1² and then generated saliency maps for every dataset from the provided head-orientation data. For the PVS-HM dataset, saliency maps were generated directly from user head-orientation recordings provided as longitude-latitude fixation points. Since the fixation data were sampled at twice the frame rate of the video (for example, 60 Hz vs. 30 Hz), we downsampled the fixation traces to match the video frame rate. For each frame, fixations were projected onto a 512×256 pixels equirectangular grid, and a Gaussian kernel with a standard deviation of 7 degrees was applied around each fixation to highlight fixation locations and produce smooth, continuous saliency maps. The contributions of all users were accumulated, and the resulting saliency maps were normalized to the range [0,1]. This process yielded one saliency map per frame, aligned with the video timeline. For the VR-EyeTracking dataset, gaze fixations were provided as normalized pixel coordinates in the range [0,1]. These fixations were first scaled to the target equirectangular resolution (512×256 pixels) and then converted into Gaussian-based saliency maps, where the Gaussian spread was computed in pixel units in order to correspond to a viewing angle of 7 degrees. To mitigate projection distortion, the intermediate saliency maps were projected into a cubemap representation, smoothed with a Gaussian filter on each cube face, and finally re-projected back into equirectangular format.

While both datasets were processed to produce 512×256 pixels saliency maps using a Gaussian kernel of size 7 degrees, the specific processing pipeline depended on the

²<https://www.ffmpeg.org/>

TABLE I: Performance comparison across Sport360 [15], PVS-HM [13], and VR-EyeTracking [14] datasets. Best results are in bold, second-best are underlined.

	Method	Sport360				PVS-HM				VR-EyeTracking			
		CC \uparrow	NSS \uparrow	KL \downarrow	AUC \uparrow	CC \uparrow	NSS \uparrow	KL \downarrow	AUC \uparrow	CC \uparrow	NSS \uparrow	KL \downarrow	AUC \uparrow
2D videos	TASED Net* [17]	0.352	1.912	—	0.883	0.651	2.413	—	0.905	0.201	2.009	—	0.864
	STSA Net* [19]	0.365	1.972	—	0.931	0.476	1.710	—	0.881	0.151	1.502	—	0.869
360-degree images	PanoSalNet \ddagger [24]	0.489	2.981	13.344	0.633	—	—	—	—	—	—	—	—
	SalGAN360* [27]	0.331	1.675	—	0.859	0.443	1.603	—	—	0.236	1.267	—	0.704
360-degree videos	Martin* [30]	0.287	1.496	—	0.851	0.215	0.828	—	0.736	0.225	2.322	—	0.865
	CP360* [34]	0.243	1.007	—	0.840	0.338	0.673	—	0.758	0.104	0.973	—	0.800
	Offline DHP* [13]	0.445	2.591	—	0.874	0.704	3.137	—	—	—	—	—	—
	Spherical U-Net* [36]	0.625	3.534	—	0.898	0.745	3.175	—	—	—	—	—	—
	Zhang360* [42]	0.620	5.125	—	0.937	0.767	3.289	—	—	—	—	—	—
	ATSal* [38]	—	—	—	—	0.564	2.489	—	0.914	0.226	2.464	—	0.869
	SST-Sal* [43]	0.439	—	8.610	—	0.424	1.244	—	0.833	<u>0.500</u>	—	<u>7.371</u>	—
	SPVP360* [39]	0.623	1.174	—	0.662	—	—	—	—	—	—	—	—
	3DSphereNet* [37]	<u>0.666</u>	4.586	<u>4.853</u>	<u>0.940</u>	0.768	3.750	<u>3.208</u>	0.933	—	—	—	—
	SVGC-AVA* [41]	—	—	—	—	0.734	3.554	—	—	—	—	—	—
	Pred360* [40]	0.656	4.381	—	0.931	0.773	3.734	—	0.934	0.291	3.768	—	0.899
	360Spred \dagger [44]	0.661	—	—	0.937	0.787	3.838	—	—	—	—	—	—
	Ours*	0.722	<u>4.746</u>	3.267	0.943	0.807	3.946	1.042	0.937	0.593	<u>3.016</u>	<u>2.334</u>	0.912

head orientation format in the original datasets. The PVS-HM dataset provided the head orientations in angular coordinates, which were directly mapped onto the sphere. In contrast, the VR-EyeTracking dataset provided the head orientation information in pixel-normalized coordinates, thus requiring cubemap smoothing to better handle projection distortions. The kernel size of 7 degrees was chosen to maintain consistency across datasets and to closely approximate the kernel used in the Sports-360 dataset (3.34 degrees for 128×256 pixels resolution), ensuring comparable saliency spread across different spatial scales.

B. Experimental Setup

For model training and testing, we used the PyTorch library [50] and an NVIDIA L40s GPU. We employed the Adam optimizer with a learning rate of 10^{-4} for the encoder and 10^{-3} for the decoder. To incorporate a regularization term and prevent overfitting, we applied a weight decay of 10^{-4} for both the encoder and decoder, along with a 30% dropout rate on the decoder side. The batch size for training and testing was set to 4. Thanks to the usage of a pretrained encoder, our model converges very fast, requiring only 6 epochs with early stopping (average of 3000 iterations to convergence). The Sport360 dataset has 2,891 iterations per epoch, while PVS-HM and VR-EyeTracking comprise 2,182 and 6,871 iterations per epoch, respectively. To avoid overfitting for the three datasets, we sampled the training set to include one every five frames. We also applied various data augmentation strategies to the dataset, such as horizontal and vertical flipping with 50% and 5% rates, respectively, to enhance the model learning capability. Furthermore, we implemented color jittering with random adjustments for brightness, contrast, and saturation, ranging from 0.7 to 1.3, to improve the model robustness against color variations [51]. We resized the 360 frames to 224×384 pixels, inspired by [46]. The parameters α and β are defined as learnable variables, with initial values empirically set to 600 and 0.15, respectively. Their learning rates were also determined through preliminary experiments, with α assigned

a learning rate of 0.1 and β set to 10^{-4} , based on observed performance improvements. The parameter k is fixed at 5.

C. Baseline methods

To evaluate our model, we compare it against a wide range of baseline methods. These include 2D saliency prediction approaches, such as TASED Net [17] and STSA Net [19]; 360-degree image saliency models, including PanoSalNet [24], SalGAN360 [27], and the method proposed by Martin *et al.* [30]; as well as video saliency prediction techniques, such as CP360 [34], Offline-DHP [13], SphericalU-Net [36], Zhang360 [42], ATSal [38], SST-Sal [43], SPVP360 [39], 3DSphereNet [37], SVGC-AVA [41], Pred360 [40], and 360Spred [44]. The numerical results for were taken directly from the original papers, with the exception of SalGAN360, SphericalU-Net, and Offline-DHP, whose results were obtained from [42]. Similarly, results for CP360, TASED Net, STSA Net, and Martin *et al.* were referenced from [40], while those for PanoSalNet were taken from [7].

D. Metrics

To evaluate our model, we employed four metrics: Kullback-Leibler Divergence (KL), CC, Normalized Scanpath Saliency (NSS), and Area Under the Curve–Judd (AUC–Judd). The CC, and KL were calculated between the ground truth and the predicted saliency maps. NSS and AUC–Judd were assessed between a binary map generated from the original fixation points and the produced saliency map, as both metrics are inherently defined with respect to human fixations. More details on these metrics can be found in [52]. The metrics were implemented in the same way as *Salient360!* benchmark [53]. To tackle distortion issues during evaluation, particularly near the poles, we adopted a latitudinal sinusoidal factor for the saliency maps during evaluation. This approach involves assigning greater weights to salient points near the equator and smaller weights to those close to the poles [53]. For a fair comparison with other state-of-the-art approaches, our results

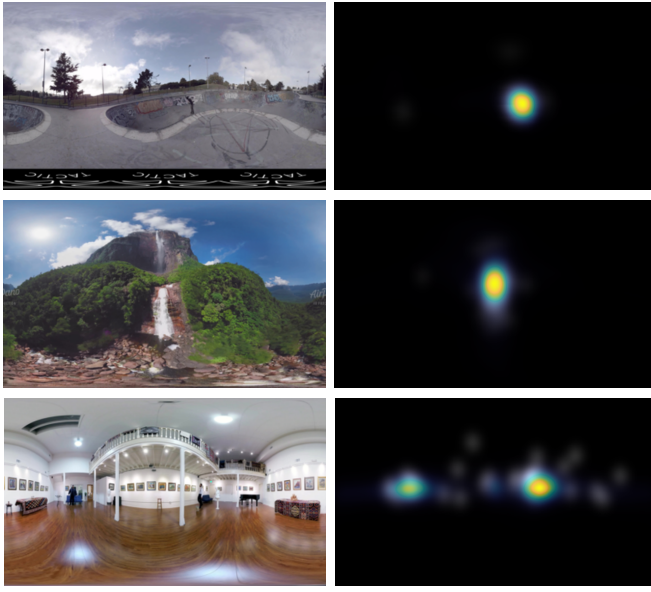


Fig. 5: Qualitative results. First row: Sport360; second row: PVS-HM; third row: VR-EyeTracking. Left: RGB input; right: ground truth (grayscale) with an overlay of the estimated saliency map (parula colormap).

in Table I adopt the following notation scheme. Methods that employed the tool with a latitudinal sinusoidal factor (default option) are marked with an asterisk (*). A dagger (\dagger) denotes methods that used the tool with uniform sampling, where evaluation metrics were calculated at uniformly sampled points on the sphere. A double dagger (\ddagger) indicates cases in which the procedure was undefined.

E. Performance Evaluation

In this section we provide both a quantitative and qualitative performance assessment of the proposed method.

1) *Quantitative results*: The performance of our model is summarized in Table I, which shows that our approach consistently outperforms all state-of-the-art methods across the three benchmark datasets in the categories of 2D videos, 360-degree images, and 360-degree videos.

In the 2D video category, the proposed model achieves substantial gains, with CC improvements of 97.8%, 24%, and 195% compared to the best prior methods on the Sport360, PVS-HM, and VR-EyeTracking datasets, respectively.

In the 360-degree image category, our model clearly outperforms image-based approaches like PanoSalNet and SalGAN360. In terms of CC, it achieves improvements of 47.6%, 82.2%, and 151.3% on Sport360, PVS-HM, and VR-EyeTracking, respectively, compared to the best-performing 360-degree image-based methods. These results highlight the effectiveness of using temporal cues in our model design.

Finally, in the 360-degree video category, our model delivers the strongest overall performance with improvements of 8.4%, 2.5%, and 18.6% in CC on the Sport360, PVS-HM, and VR-EyeTracking datasets, respectively, compared to prior works. The only exceptions are noted in the NSS metric, where our

TABLE II: Comparison of model complexity and computational efficiency across models.

Model	Parameters (M) \downarrow	FLOPs \downarrow	Model Size \downarrow
Offline DHP [13]	34.00	—	—
SalGAN360 [27]	31.78	—	—
Spherical U-Net [36]	12.30	—	—
SST-Sal [43]	8.32	768.0K	225.4K
SPVP360 [39]	7.72	—	—
360Spred [44]	7.59	—	—
CP360 [34]	—	105.8G	360.0M
TASED Net [17]	—	91.8G	85.4M
Martin [30]	—	<u>27.9M</u>	11.7M
ATSal [38]	—	277.2G	383.6M
STSA Net [19]	—	193.7G	643.9M
Pred360 [40]	—	306.5M	1.0M
Ours	3.70	1.21G	14.13M

model ranks second behind Zhang360 on the Sport360 dataset and behind Pred360 on VR-EyeTracking.

These results demonstrate that our model consistently improves saliency prediction accuracy across diverse datasets compared to several recent state-of-the-art approaches.

2) *Qualitative results*: To visually validate the effectiveness of our model, we present three randomly selected samples from the three datasets in Figures 5. The left column shows the input RGB video frame, and the right column presents the corresponding grayscale ground-truth saliency map with an overlay of the estimated saliency map (parula colormap). As clearly shown by the figure, our model successfully predicts accurate saliency maps across different datasets, providing clear evidence of its effectiveness.

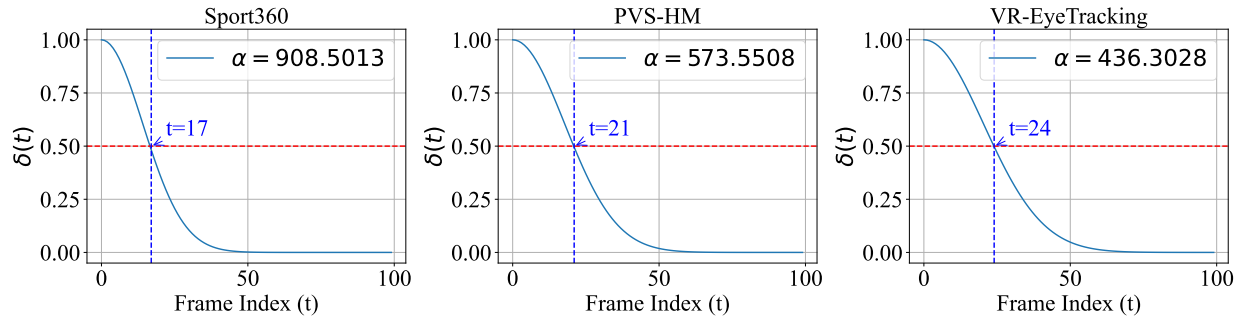
3) *Model complexity and computational efficiency*: Table II presents a comparison of model complexity and computational efficiency for recent 360-degree video saliency prediction methods, with results sourced from [40] [44]. Our proposed model is notably lightweight, comprising only 3.70 million parameters and requiring 14.13 MB of storage, while achieving a competitive computational cost of 1.21 GFLOPs. Based on Table II, and in comparison with other state-of-the-art approaches, our model has the lowest number of parameters and ranks fourth in terms of FLOPs and model size.

This compact design makes our method particularly well-suited for edge-side or client-side deployment, where computational resources and memory are limited (*e.g.*, in VR headsets). Our approach strikes a balance between lightweight design, accuracy, and efficiency, enabling real-time saliency estimation directly on user devices. Additionally, we measured the average inference time of our model to be 5.1ms per frame, corresponding to a throughput of approximately 196 frames per second (fps) on the hardware described in the experimental setup. This confirms the high efficiency of the model and provides strong evidence that it can operate seamlessly in real-time applications, like viewport prediction, without introducing noticeable latency.

V. ABLATION STUDY

A. Viewing Center Bias contribution

Table III presents an ablation study done across three datasets (Sport360, PVS-HM, and VR-EyeTracking) to eval-

Fig. 6: Temporal Decay of $\delta(t)$ Function across Frame Indices for Each DatasetTABLE III: Ablation study across datasets showing the impact of Center Bias through δ and β components.

$\delta(\cdot)$	β	CC \uparrow	NSS \uparrow	KL \downarrow	AUC Judd \uparrow
Sport360					
\times	\times	0.696	4.482	3.461	0.941
\times	\checkmark	0.707	4.537	3.372	0.942
\checkmark	\times	0.716	4.647	3.303	0.943
\checkmark	\checkmark	0.722	4.746	3.267	0.943
PVS-HM					
\times	\times	0.768	3.649	1.254	0.933
\times	\checkmark	0.790	3.827	1.139	0.935
\checkmark	\times	0.776	3.720	1.120	0.936
\checkmark	\checkmark	0.807	3.946	1.042	0.937
VR-EyeTracking					
\times	\times	0.570	2.780	2.461	0.910
\times	\checkmark	0.581	2.884	2.464	0.911
\checkmark	\times	0.586	2.992	2.432	0.912
\checkmark	\checkmark	0.593	3.016	2.334	0.912

ate the contribution of the CB on our model through δ and β components.

The results clearly show that both δ and β contribute to the performance improvement across all datasets, though with varying degrees of impact. Removing one of these components leads to performance degradation across all metrics, while removing both components results in the lowest overall accuracy.

On the Sport360 dataset, the β component has a smaller influence compared to δ , indicating that this dataset exhibits a weaker long-range dependence on center bias. In contrast, the PVS-HM dataset shows a significant performance drop when the β is removed, suggesting a stronger reliance on persistent center bias. These findings align with observations reported in [37], which highlight that PVS-HM demonstrates a more center-biased behavior across its videos than Sport360. On the other hand, Sport360 appears to rely more on δ , as the center bias primarily occurs at the beginning of the videos, likely due to the characteristics of the content within this dataset.

In the VR-EyeTracking dataset, the benefits of both δ and β are evident. Each component individually leads to improvements in evaluation metrics, especially in CC and NSS, while their combination consistently yields the strongest results, with a CC of 0.593, NSS of 3.016, and KL divergence of 2.334. Here, the contributions of δ and β are nearly equal, indicating that the VR-EyeTracking dataset exhibits a balance between early frame-centered viewing behavior and sustained

TABLE IV: Learned values for α and β parameters across datasets.

Dataset	α	β
Sport360	908.5013	0.0030
PVS-HM	573.5508	0.1773
VR-EyeTracking	436.3028	0.1079

TABLE V: Performance comparison across different loss configurations.

\mathcal{L}_{CC}	\mathcal{L}_{KL}	\mathcal{L}_{SMSE}	\mathcal{L}_{BCE}	CC \uparrow	NSS \uparrow	KL \downarrow	AUC Judd \uparrow
\checkmark	\times	\times	\times	0.780	3.786	0.967	0.934
\times	\checkmark	\times	\times	0.778	3.725	1.236	0.935
\checkmark	\checkmark	\times	\times	0.798	3.869	1.117	0.937
\checkmark	\checkmark	\checkmark	\times	0.803	3.927	1.064	0.936
\checkmark	\checkmark	\checkmark	\checkmark	0.807	3.946	1.042	0.937

central attention patterns.

Overall, these results confirm that both δ and β are important for modeling realistic viewing behavior. Specifically, δ aligns predictions with the natural tendency of users to focus on the center at the beginning of a video, while β accounts for the global bias during viewing. Together, they provide complementary benefits, leading to consistently improved saliency predictions across all datasets. Furthermore, the contributions of δ and β can vary from one dataset to another, highlighting the importance of integrating these components and incorporating them as learnable parameters within the model. This allows for adaptation based on the content of each dataset.

To further analyze the contribution of δ and β components in our model, Table IV presents the final values of the parameters α and β after convergence across the three datasets. As observed, the value of α decreases below its initial setting of 600 in the PVS-HM and VR-EyeTracking datasets, indicating that the relative contribution of δ increases in these datasets. In contrast, for the Sport360 dataset, α increases to 908.5, suggesting that the model reduces the influence of δ . This behavior implies that PVS-HM and VR-EyeTracking exhibit stronger initial fixation tendencies, whereas Sport360 is less dependent on δ . To further illustrate the contribution of δ , Figure 6 plots the δ function across frame indices using the learned α values. The frame index corresponding to a δ of 0.5 has been highlighted. In Sport360, δ is equal to 0.5 at frame 17, compared to frame 21 in PVS-HM and frame 24 in VR-EyeTracking. These results confirm that VR-EyeTracking

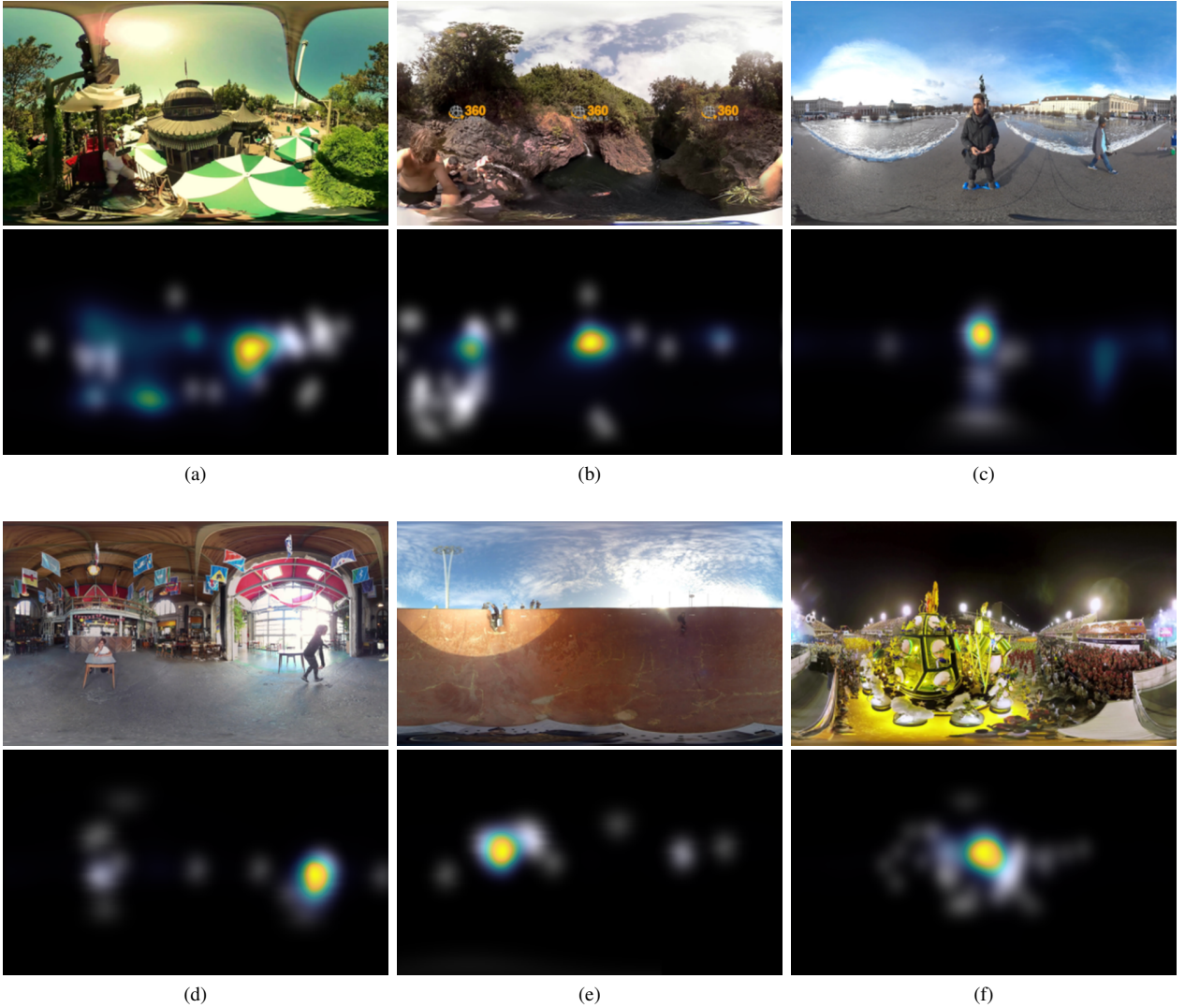


Fig. 7: Qualitative Analysis of Challenging Examples. Up: frames extracted from the three datasets; Down: ground-truth saliency maps (grayscale) with an overlay of the saliency maps predicted with the proposed method (parula colormaps).

demonstrates the strongest δ dependence, followed by PVS-HM, while Sport360 shows the weakest. Regarding the β contribution, the parameter β increases from its initial value of 0.15 to 0.17 in the PVS-HM dataset, indicating that the model strengthens the influence of the long-range center bias. In contrast, β slightly decreases to 0.11 for VR-EyeTracking, showing a moderate but still relevant β effect. For Sport360, however, β drops to 0.003, suggesting that long-range center bias has minimal influence in this dataset compared to others.

B. Loss selection

To highlight the contribution of each component in our loss function, we conducted an ablation study on the PVS-HM dataset by training and testing the model under different loss configurations (see Table V). The results show that each loss plays an important role in improving the performance. Specifically, training the model with only the correlation loss \mathcal{L}_{CC} or \mathcal{L}_{KL} divergence loss yields good results, but combining them

$\mathcal{L}_{CC} + \mathcal{L}_{KL}$ leads to a noticeable improvement across CC, NSS, and AUC metrics. Adding the \mathcal{L}_{SMSE} further enhances the consistency of predictions, as reflected in higher CC and NSS scores and lower KL divergence. Finally, integrating the binary cross-entropy loss \mathcal{L}_{BCE} , the model achieves the best overall performance, with the highest CC (0.807), NSS (3.946), and AUC-Judd (0.937). Additionally, it results in a lower KL divergence of 1.042 compared to other loss functions, except for \mathcal{L}_{CC} , which has the lowest KL divergence among all the losses evaluated. A likely explanation is that optimizing solely with \mathcal{L}_{CC} enforces a strong correlation between predicted and ground-truth maps, which closely align their distributions. This could explain the low value of the KL divergence, even though this loss does not yield the best overall performance across other metrics.

C. Qualitative analysis of challenging examples

Although our model outperforms existing state-of-the-art approaches on widely used datasets, several challenging cases

with reduced prediction accuracy remain, as illustrated in Figure 7. The figure shows six frames extracted from the three datasets (upper rows) and the corresponding ground-truth saliency maps in gray scale with an overlay in parula colormap of the estimated saliency maps (lower rows).

In Figure 7a, we show frame 546 from video 63 in the VR-EyeTracking dataset, recorded during an amusement park ride where the entire content changes rapidly from frame to frame with many points of interest inside the scene. Our model estimates salient areas primarily around the center, while the ground-truth maps reveal user fixations distributed across multiple regions, reflecting the difficulty of scenes with many simultaneous points of interest.

In Figure 7b, we show frame 246 from video 24 of the VR-EyeTracking dataset. This video briefly displays an advertising logo (“360 Labs”), which disappears after a few seconds. Our model incorrectly detected the logo region as salient, overshadowing the main content. Moreover, the scene itself contained several competing points of interest, leading to user fixations scattered across the panorama, which our model struggled to predict accurately.

In Figure 7c, depicting frame 53 of video 250 in the Sport360 dataset, two individuals appear in the scene. The ground-truth map shows strong focus on the central person, but our model distributed saliency between both individuals: one in the center moving his hands, and the other on the right who is moving across the scene. Comparable situations are also observed in the Sport360 dataset in Figure 7d (frame 230 of video 301) and Figure 7e (frame 286 of video 244), where the model prioritizes one salient region over another.

Finally, in Figure 7f, we present frame 374 from the RioOlympics video in the PVS-HM dataset. This video contains numerous people moving across the scene, creating complex motion patterns. While our model captured saliency regions to some extent, its predictions were less precise compared to the ground truth. Additionally, the video is composed of multiple stitched segments, causing frequent scene changes that further complicate saliency estimation.

VI. FUTURE DIRECTIONS

From a modeling perspective, there is still a strong need for more accurate, lightweight saliency estimation models suitable for real-time applications. This is especially critical for tasks such as viewport prediction, where high-quality saliency maps directly translate into better prediction performance as demonstrated in [5]. Furthermore, future models should integrate richer feature representations, such as spatial and temporal complexity cues or other type of information, to achieve faster convergence and enhance the accuracy of attention modeling across diverse 360-degree video content.

Another important direction is to train our model on a wider range of datasets containing more diverse videos to improve its generalization capability and reliability. To achieve this, the creation of new large-scale datasets that capture a wider variety of scenes and are annotated with eye-tracking data from a larger and more diverse pool of users is needed. Such datasets would help mitigate bias and ensure that models remain robust under different viewing conditions and content types.

Finally, based on our observations of the contribution of center viewing bias, further studies and experiments are needed to better understand how this bias influences attention in 360-degree videos. Incorporating these insights into future models could lead to more accurate saliency estimation.

VII. CONCLUSION

In this paper, we propose SalFormer360, a transformer-based model for saliency estimation in 360-degree videos. By customizing the SegFormer backbone and designing a tailored decoder with additional priors, our model effectively shows high capability to predict the saliency maps for 360-degree videos. Experimental results across three large-scale benchmark datasets demonstrate that SalFormer360 consistently outperforms state-of-the-art methods, achieving improvements of up to 18.6% in CC. SalFormer360 is a lightweight model with low computational requirements, which makes it well-suited for real-time applications such as viewport prediction, and has the capability to be deployed on edge devices or client-side devices like head-mounted displays, enabling practical integration into immersive media systems.

REFERENCES

- [1] ITU-T, “F.743-10 - Requirements for mobile edge computing-enabled content delivery networks,” International Telecommunication Union (ITU), Tech. Rep., 2019.
- [2] F. Battisti, S. Baldoni, M. Brizzi, and M. Carli, “A feature-based approach for saliency estimation of omni-directional images,” *Signal Processing: Image Communication*, vol. 69, pp. 53–59, 2018, salient360: Visual attention modeling for 360° Images. [Online]. Available: <https://www.sciencedirect.com/science/article/pii/S092359651830242X>
- [3] A. Ao and S. Park, “Applying Transformer-Based Computer Vision Models to Adaptive Bitrate Allocation for 360° Live Streaming,” in *2024 IEEE Wireless Communications and Networking Conference (WCNC)*, 2024, pp. 1–6.
- [4] A. Nguyen and Z. Yan, “Enhancing 360 video streaming through salient content in head-mounted displays,” *Sensors*, vol. 23, no. 8, 2023. [Online]. Available: <https://www.mdpi.com/1424-8220/23/8/4016>
- [5] M. F. R. Rondón, L. Sassatelli, R. Aparicio-Pardo, and F. Precioso, “Track: A new method from a re-examination of deep architectures for head motion prediction in 360° videos,” *IEEE Transactions on Pattern Analysis and Machine Intelligence*, vol. 44, no. 9, pp. 5681–5699, 2022.
- [6] C.-L. Fan, S.-C. Yen, C.-Y. Huang, and C.-H. Hsu, “Optimizing fixation prediction using recurrent neural networks for 360° video streaming in head-mounted virtual reality,” *IEEE Transactions on Multimedia*, vol. 22, no. 3, pp. 744–759, 2020.
- [7] S. Peng, J. Hu, Z. Li, H. Xiao, S. Yang, and C. Xu, “Spherical convolution-based saliency detection for fov prediction in 360-degree video streaming,” in *2023 International Wireless Communications and Mobile Computing (IWCMC)*, 2023, pp. 162–167.
- [8] M. Wang, S. Peng, X. Chen, Y. Zhao, M. Xu, and C. Xu, “CoLive: An Edge-Assisted Online Learning Framework for Viewport Prediction in 360°Live Streaming,” in *2022 IEEE International Conference on Multimedia and Expo (ICME)*, 2022, pp. 1–6.
- [9] H. Wang, Z. Long, H. Dong, and A. El Saddik, “MADRL-Based Rate Adaptation for 360°Video Streaming With Multiviewpoint Prediction,” *IEEE Internet of Things Journal*, vol. 11, no. 15, pp. 26503–26517, 2024.
- [10] L. Zhang, H. Zhou, L. Shen, J. Liu, and L. Cui, “Towards attention-aware interactive 360-degree video streaming on smartphones,” *IEEE Network*, pp. 1–1, 2025.
- [11] M. Setayesh and V. W. S. Wong, “Viewport prediction, bitrate selection, and beamforming design for thz-enabled 360°video streaming,” *IEEE Transactions on Wireless Communications*, vol. 24, no. 3, pp. 1849–1865, 2025.
- [12] E. Xie, W. Wang, Z. Yu, A. Anandkumar, J. M. Álvarez, and P. Luo, “Segformer: Simple and efficient design for semantic segmentation with transformers,” *CoRR*, vol. abs/2105.15203, 2021. [Online]. Available: <https://arxiv.org/abs/2105.15203>

- [13] M. Xu, Y. Song, J. Wang, M. Qiao, L. Huo, and Z. Wang, "Predicting head movement in panoramic video: A deep reinforcement learning approach," *IEEE Transactions on Pattern Analysis and Machine Intelligence*, vol. PP, pp. 1–1, 07 2018.
- [14] Y. Xu, Y. Dong, J. Wu, Z. Sun, Z. Shi, J. Yu, and S. Gao, "Gaze Prediction in Dynamic 360° Immersive Videos," in *2018 IEEE/CVF Conference on Computer Vision and Pattern Recognition*, 2018, pp. 5333–5342.
- [15] Z. Zhang, Y. Xu, J. Yu, and S. Gao, "Saliency Detection in 360° Videos," in *Proceedings of the European Conference on Computer Vision (ECCV)*, September 2018.
- [16] J. Lou, H. Lin, D. Marshall, D. Saupe, and H. Liu, "TranSalNet: Towards perceptually relevant visual saliency prediction," *Neurocomputing*, vol. 494, p. 455–467, jul 2022. [Online]. Available: <http://dx.doi.org/10.1016/j.neucom.2022.04.080>
- [17] K. Min and J. Corso, "Tased-net: Temporally-aggregating spatial encoder-decoder network for video saliency detection," 08 2019. [Online]. Available: <https://arxiv.org/abs/1908.05786>
- [18] Z. Wang, Z. Liu, L. Gongyang, Y. Wang, T. Zhang, L. Xu, and J. Wang, "Spatio-temporal self-attention network for video saliency prediction," *IEEE Transactions on Multimedia*, vol. PP, pp. 1–1, 12 2021.
- [19] W. Wang, J. Shen, J. Xie, M.-M. Cheng, H. Ling, and A. Borji, "Revisiting video saliency prediction in the deep learning era," *IEEE Transactions on Pattern Analysis and Machine Intelligence*, vol. 43, no. 1, pp. 220–237, 2021.
- [20] X. Wu, Z. Wu, J. Zhang, and L. Ju, "Salsac: A video saliency prediction model with shuffled attentions and correlation-based convlstm," *Proceedings of the AAAI Conference on Artificial Intelligence*, vol. 34, pp. 12410–12417, 04 2020.
- [21] R. Drost, J. Jiao, and J. Noble, *Unified Image and Video Saliency Modeling*. Springer-Verlag, 10 2020, pp. 419–435.
- [22] A. G. Howard, M. Zhu, B. Chen, D. Kalenichenko, W. Wang, T. Weyand, M. Andreetto, and H. Adam, "Mobilenets: Efficient convolutional neural networks for mobile vision applications," 2017. [Online]. Available: <https://arxiv.org/abs/1704.04861>
- [23] S. Baldoni, O. Poci, G. Calvagno, and F. Battisti, "An Ablation Study on 360-Degree Saliency Estimation," in *2023 International Symposium on Image and Signal Processing and Analysis (ISPA)*, 2023, pp. 1–6.
- [24] A. Nguyen, Z. Yan, and K. Nahrstedt, "Your Attention is Unique: Detecting 360-Degree Video Saliency in Head-Mounted Display for Head Movement Prediction," in *Proceedings of the 26th ACM International Conference on Multimedia*, ser. MM '18. New York, NY, USA: Association for Computing Machinery, 2018, p. 1190–1198.
- [25] M. F. R. Rondón, L. Sassielli, R. A. Pardo, and F. Precioso, "Track: a Multi-Modal Deep Architecture for Head Motion Prediction in 360°Videos," in *2020 IEEE International Conference on Image Processing (ICIP)*, 2020, pp. 2586–2590.
- [26] Y. Tian, Y. Zhong, Y. Han, and F. Chen, "Viewport prediction with cross modal multiscale transformer for 360°video streaming," *Scientific Reports*, vol. 15, 08 2025.
- [27] F.-Y. Chao, L. Zhang, W. Hamidouche, and O. Déforges, "Salgan360: Visual saliency prediction on 360 degree images with generative adversarial networks," in *2018 IEEE International Conference on Multimedia & Expo Workshops (ICMEW)*, 07 2018.
- [28] J. Pan, C. C. Ferrer, K. McGuinness, N. E. O'Connor, J. Torres, E. Sayrol, and X. G. i Nieto, "Salgan: Visual saliency prediction with generative adversarial networks," 2018. [Online]. Available: <https://arxiv.org/abs/1701.01081>
- [29] I. J. Goodfellow, J. Pouget-Abadie, M. Mirza, B. Xu, D. Warde-Farley, S. Ozair, A. Courville, and Y. Bengio, "Generative adversarial networks," 2014. [Online]. Available: <https://arxiv.org/abs/1406.2661>
- [30] D. Martin, A. Serrano, and B. Masia, "Panoramic convolutions for 360° single-image saliency prediction," in *CVPR Workshop on Computer Vision for Augmented and Virtual Reality*, 2020.
- [31] B. Coors, A. P. Condurache, and A. Geiger, "Spherenet: Learning spherical representations for detection and classification in omnidirectional images," in *Proceedings of the European Conference on Computer Vision (ECCV)*, September 2018.
- [32] M. Z. A. Wahba, S. Baldoni, and F. Battisti, "Sphere-GAN: a GAN-based Approach for Saliency Estimation in 360°Videos," 2025. [Online]. Available: <https://arxiv.org/abs/2509.11948>
- [33] O. Ronneberger, P. Fischer, and T. Brox, "U-net: Convolutional networks for biomedical image segmentation," 2015. [Online]. Available: <https://arxiv.org/abs/1505.04597>
- [34] H.-T. Cheng, C.-H. Chao, J.-D. Dong, H.-K. Wen, T.-L. Liu, and M. Sun, "Cube padding for weakly-supervised saliency prediction in 360° videos," 2018. [Online]. Available: <https://arxiv.org/abs/1806.01320>
- [35] X. Shi, Z. Chen, H. Wang, D.-Y. Yeung, W. kin Wong, and W. chun Woo, "Convolutional lstm network: A machine learning approach for precipitation nowcasting," 2015. [Online]. Available: <https://arxiv.org/abs/1506.04214>
- [36] Z. Zhang, Y. Xu, J. Yu, and S. Gao, "Saliency detection in 360°videos," in *Computer Vision – ECCV 2018: 15th European Conference, Munich, Germany, September 8–14, 2018, Proceedings, Part VII*. Berlin, Heidelberg: Springer-Verlag, 2018, p. 504–520. [Online]. Available: https://doi.org/10.1007/978-3-030-01234-2_30
- [37] P.-W. Chen, T.-S. Yang, G.-L. Huang, C.-W. Huang, Y.-C. Chao, C.-H. Lu, and P.-Y. Wu, "Viewing bias matters in 360° videos visual saliency prediction," *IEEE Access*, vol. 11, pp. 46084–46094, 2023.
- [38] Y. Dahou, M. Tliba, K. McGuinness, and N. O'Connor, "Atsal: An attention based architecture for saliency prediction in 360 videos," 2020. [Online]. Available: <https://arxiv.org/abs/2011.10600>
- [39] J. Li, L. Han, C. Zhang, Q. Li, and Z. Liu, "Spherical convolution empowered fov prediction in 360-degree video multicast with limited fov feedback," 2022. [Online]. Available: <https://arxiv.org/abs/2201.12525>
- [40] Z. Wan, H. Qin, R. Xiong, Z. Li, X. Fan, and D. Zhao, "Predicting 360° video saliency: A convlstm encoder-decoder network with spatio-temporal consistency," *IEEE Journal on Emerging and Selected Topics in Circuits and Systems*, vol. 14, no. 2, pp. 311–322, 2024.
- [41] Q. Yang, Y. Li, C. Li, H. Wang, S. Yan, L. Wei, W. Dai, J. Zou, H. Xiong, and P. Frossard, "Svgec-ava: 360-degree video saliency prediction with spherical vector-based graph convolution and audio-visual attention," *Trans. Multi.*, vol. 26, p. 3061–3076, Jan. 2024. [Online]. Available: <https://doi.org/10.1109/TMM.2023.3306596>
- [42] Y. Zhang, F. Dai, Y. Ma, H. Li, Q. Zhao, and Y. Zhang, "Saliency prediction network for 360° videos," *IEEE Journal of Selected Topics in Signal Processing*, vol. 14, no. 1, pp. 27–37, 2020.
- [43] E. Bernal-Berdun, D. Martin, D. Gutierrez, and B. Masia, "Sst-sal: A spherical spatio-temporal approach for saliency prediction in 360°videos," *Computers & Graphics*, vol. 106, pp. 200–209, 2022. [Online]. Available: <https://www.sciencedirect.com/science/article/pii/S0097849322001042>
- [44] Q. Yang, W. Gao, C. Li, H. Wang, W. Dai, J. Zou, H. Xiong, and P. Frossard, "360spredd: Saliency prediction for 360-degree videos based on 3d separable graph convolutional networks," *IEEE Transactions on Circuits and Systems for Video Technology*, vol. 34, no. 10, pp. 9979–9996, 2024.
- [45] Q. Yang, C. Li, W. Dai, J. Zou, G.-J. Qi, and H. Xiong, "Rotation equivariant graph convolutional network for spherical image classification," in *Proceedings of the IEEE/CVF Conference on Computer Vision and Pattern Recognition (CVPR)*, June 2020.
- [46] P.-W. Chen, T.-S. Yang, G.-L. Huang, C.-W. Huang, Y.-C. Chao, C.-H. Lu, and P.-Y. Wu, "Viewing bias matters in 360° videos visual saliency prediction," *IEEE Access*, vol. PP, pp. 1–1, 01 2023.
- [47] A. Vaswani, N. Shazeer, N. Parmar, J. Uszkoreit, L. Jones, A. N. Gomez, L. Kaiser, and I. Polosukhin, "Attention is all you need," 2023. [Online]. Available: <https://arxiv.org/abs/1706.03762>
- [48] J. Deng, W. Dong, R. Socher, L.-J. Li, K. Li, and L. Fei-Fei, "Imagenet: A large-scale hierarchical image database," in *2009 IEEE Conference on Computer Vision and Pattern Recognition*, 2009, pp. 248–255.
- [49] B. Zhou, H. Zhao, X. Puig, T. Xiao, S. Fidler, A. Barriuso, and A. Torralba, "Semantic understanding of scenes through the ade20k dataset," 2018. [Online]. Available: <https://arxiv.org/abs/1608.05442>
- [50] A. Paszke, S. Gross, F. Massa, A. Lerer, J. Bradbury, G. Chanan, T. Killeen, Z. Lin, N. Gimelshein, L. Antiga, A. Desmaison, A. Kopf, E. Yang, Z. DeVito, M. Raison, A. Tejani, S. Chilamkurthy, B. Steiner, L. Fang, J. Bai, and S. Chintala, "Pytorch: An imperative style, high-performance deep learning library," 2019. [Online]. Available: <https://arxiv.org/abs/1912.01703>
- [51] TorchVision, maintainers and contributors, "Torchvision: Pytorch's computer vision library [software]," Available: <https://github.com/pytorch/vision>, 2016.
- [52] Z. Bylinskii, T. Judd, A. Oliva, A. Torralba, and F. Durand, "What do different evaluation metrics tell us about saliency models?" *IEEE Transactions on Pattern Analysis and Machine Intelligence*, vol. 41, no. 3, pp. 740–757, 2019.
- [53] J. Gutiérrez, E. J. David, A. Coutrot, M. P. Da Silva, and P. L. Callet, "Introducing un salient360! benchmark: A platform for evaluating visual attention models for 360° contents," in *2018 Tenth International Conference on Quality of Multimedia Experience (QoMEX)*, 2018, pp. 1–3.